Electrochemical tuning of vertically aligned MoS_2 nanofilms and its application in improving hydrogen evolution reaction

Haotian Wang[a], Zhiyi Lu[b], Shicheng Xu[c], Desheng Kong[b], Judy J. Cha[b], Guangyuan Zheng[d], Po-Chun Hsu[b], Kai Yan[b], David Bradshaw[b], Fritz B. Prinz[b,c], and Yi Cui[b,e,1]

Departments of [a]Applied Physics, [b]Materials Science and Engineering, [c]Mechanical Engineering, and [d]Chemical Engineering, Stanford University, Stanford, CA 94305; and [e]Stanford Institute for Materials and Energy Sciences, SLAC National Accelerator Laboratory, Menlo Park, CA 94025

Edited by Charles M Lieber, Harvard University, Cambridge, MA, and approved October 30, 2013 (received for review September 5, 2013)

The ability to intercalate guest species into the van der Waals gap of 2D layered materials affords the opportunity to engineer the electronic structures for a variety of applications. Here we demonstrate the continuous tuning of layer vertically aligned MoS_2 nanofilms through electrochemical intercalation of Li^+ ions. By scanning the Li intercalation potential from high to low, we have gained control of multiple important material properties in a continuous manner, including tuning the oxidation state of Mo, the transition of semiconducting 2H to metallic 1T phase, and expanding the van der Waals gap until exfoliation. Using such nanofilms after different degree of Li intercalation, we show the significant improvement of the hydrogen evolution reaction activity. A strong correlation between such tunable material properties and hydrogen evolution reaction activity is established. This work provides an intriguing and effective approach on tuning electronic structures for optimizing the catalytic activity.

2D materials | layer vertically standing | electrochemical catalysis

Layer-structured 2D materials are an interesting family of materials with strong covalent bonding within molecular layers and weak van der Waals interaction between layers. Beyond intensively studied graphene-related materials (1–4), there has been recent strong interest in other layered materials whose vertical thickness can be thinned down to less than few nanometers and horizontal width can also be reduced to nanoscale (5–9). The strong interest is driven by their interesting physical and chemical properties (2, 10) and their potential applications in transistors, batteries, topological insulators, thermoelectrics, artificial photosynthesis, and catalysis (4, 11–25).

One of the unique properties of 2D layered materials is their ability to intercalate guest species into their van der Waals gaps, opening up the opportunities to tune the properties of materials. For example, the spacing between the 2D layers could be increased by intercalation such as lithium (Li) intercalated graphite or molybdenum disulfide (MoS_2) and copper intercalated bismuth selenide (26–29). The electronic structures of the host lattice, such as the charge density, anisotropic transport, oxidation state, and phase transition, may also be changed by different species intercalation (26, 27).

As one of the most interesting layered materials, MoS_2 has been extensively studied in a variety of areas such as electrocatalysis (20–22, 30–36). It is known that there is a strong correlation between the electronic structure and catalytic activity of the catalysts (20, 37–41). It is intriguing to continuously tune the morphology and electronic structure of MoS_2 and explore the effects on MoS_2 hydrogen evolution reaction (HER) activity. Very recent studies demonstrated that the monolayered MoS_2 and WS_2 nanosheets with 1T metallic phase synthesized by chemical exfoliation exhibited superior HER catalytic activity to those with 2H semiconducting phase (35, 42), with a possible explanation that the strained 1T phase facilitates the hydrogen binding process during HER (42). However, it only offers two end states of materials and does not offer a continuous tuning. A systematic investigation to correlate the gradually tuned electronic structure, including oxidation state shift and semiconducting–metallic phase transition, and the corresponding HER activity is important but unexplored. We believe that the Li electrochemical intercalation method offers a unique way to tune the catalysts for optimization.

In this paper, we demonstrate that the layer spacing, oxidation state, and the ratio of 2H semiconducting to 1T metallic phase of MoS_2 HER catalysts were continuously tuned by Li intercalation to different voltages vs. Li^+/Li in nanofilms with molecular layers perpendicular to the substrates. Correspondingly, the catalytic activity for HER was observed to be continuously tuned. The lower oxidation state of Mo and 1T metallic phase of MoS_2 turn out to have better HER catalytic activities. The performance of MoS_2 catalyst on both flat and 3D electrodes was dramatically improved when it was discharged to low potentials vs. Li^+/Li.

Results

Synthesis and Characterization. The atomic structure of 2H MoS_2 is illustrated in Fig. 1*A*. Charge neutral molecular layers consisting of covalently bonded Mo and S atoms stack along the *z* direction by weak van der Waals interaction. To largely expose the active edge sites for HER (20, 21, 43), MoS_2 nanofilms on mirror polished glassy carbon (MPGC) with molecular layers perpendicular to the substrate were converted from 12-nm Mo film by a rapid sulfurization process presented in our previous work (43, 44) (*Materials and Methods*), as illustrated by the

Significance

The electronic structures of two-dimensional materials can be tuned for a variety of applications by guest species intercalation into the van der Waals gaps. Using Li electrochemical intercalated MoS_2 as an example here, we correlate the continuously tuned electronic structure of lithiated MoS_2 with the corresponding enhanced hydrogen evolution reaction activity, and thus construct the electronic structure–catalytic activity relationship. This work offers a unique thinking of tuning the electronic structures of layered materials by guest species intercalation for optimizing different kinds of catalysis on the basis of the strong correlation between the electronic structures and catalytic activities of the catalysts.

Author contributions: H.W., D.K., F.B.P., and Y.C. designed research; H.W., Z.L., S.X., J.J.C., G.Z., P.-C.H., and D.B. performed research; H.W., Z.L., S.X., F.B.P., and Y.C. contributed new reagents/analytic tools; H.W., Z.L., D.K., J.J.C., G.Z., P.-C.H., K.Y., F.B.P., and Y.C. analyzed data; and H.W., Z.L., S.X., D.K., J.J.C., and Y.C. wrote the paper.

The authors declare no conflict of interest.

This article is a PNAS Direct Submission.

[1]To whom correspondence should be addressed. E-mail: yicui@stanford.edu.

This article contains supporting information online at www.pnas.org/lookup/suppl/doi:10.1073/pnas.1316792110/-/DCSupplemental.

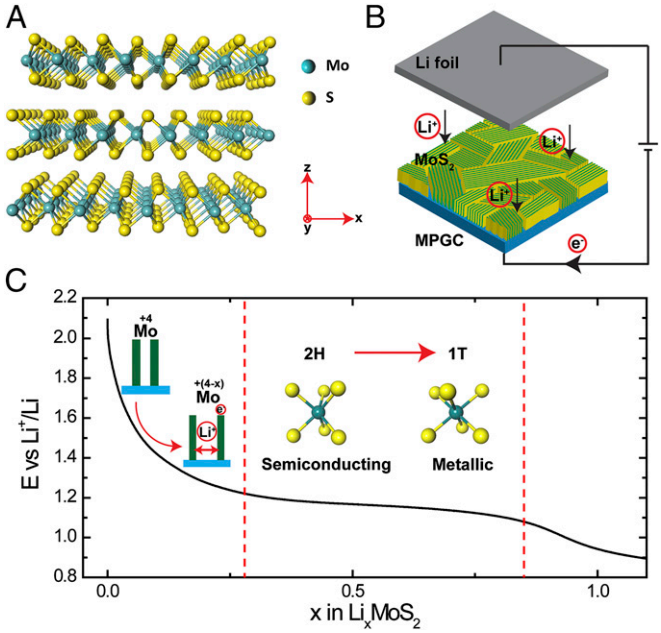

Fig. 1. Schematics and galvanostatic discharge curve of Li electrochemical intercalation into MoS_2 nanofilms. (*A*) Crystal structure of 2H MoS_2. (*B*) Schematic of the battery testing system. The cathode is MoS_2 nanofilm with molecular layers perpendicular to the substrate, where the green and yellow colors represent the edge sites and the terrace sites, respectively. The anode is the Li foil. (*C*) Galvanostatic discharge curve representing the lithiation process. Li intercalates into the van der Waals gaps of MoS_2 to donate electrons to the slabs and expand the layer spacing. The voltage monotonically drops to 1.2 V vs. Li^+/Li to reach a Li content of 0.28, after which the system undergoes a 2H to 1T MoS_2 first-order phase transition. The atomic structure is changed from trigonal prismatic to octahedral, along with the electronic semiconducting to metallic transition.

schematic in Fig. 1*B*. The as-grown MoS_2 nanofilm together with a piece of Li foil were then made into a pouch battery cell to perform Li electrochemical intercalation through a galvanostatic discharge process and form Li_xMoS_2 compound (*Materials and Methods*). The battery testing system enabled us to monitor and control the lithiation process at room temperature within only several hours, by which the amount of intercalated Li was continuously tuned as shown in Fig. 1*C* (29, 45). The discharge curve in Fig. 1*C* offers us useful information about the tuning of electronic structure of MoS_2 during Li intercalation. The voltage of Li_xMoS_2 vs. Li^+/Li is decreased monotonically from 2.1 to 1.2 V, during which Li intercalates into MoS_2 with the content x increasing to around 0.28 (29, 46). The following lithiation process undergoes a 2H to 1T MoS_2 first-order phase transition, as a well-defined discharge plateau is observed between 1.2 and 1.1 V in Fig. 1*C* (29, 45–47). The 2H and 1T MoS_2 have different atomic and electronic structures illustrated in Fig. 1*C*. In 2H MoS_2, which is semiconducting, the Mo atom is coordinated by six S atoms in a trigonal prismatic arrangement, whereas the Mo atom in the 1T phase presents an octahedral S coordination which results in the metallic property (29, 35, 42, 47, 48). Despite the electronic structure change, because the Li between the layers is expected to expand the layer spacing as indicated in Fig. 1*C*, the morphology of the as-grown MoS_2 nanofilm can also be tuned by the lithiation process (29, 45).

Characterizations of MoS_2 nanofilms stopped at different lithiation voltages were performed after the surface contaminations were removed by ethanol treatment. Different from the recent study of completely exfoliated WS_2 monolayers in which Li was not detected (42), electron energy loss spectroscopy (Fig. S1) and inductively coupled plasma mass spectroscopy (ICP-MS) (*Materials and Methods*; Table S1) results suggest that only part of the intercalated Li in our MoS_2 layers vertically aligned structure reacts with ethanol. The tuning of MoS_2 layer spacing by Li electrochemical intercalation is confirmed by the transmission electron microscopy (TEM) images of MoS_2 discharged to different voltages in Fig. 2. Pristine MoS_2 nanofilm on MPGC with molecular layers perpendicular to the substrate is shown in Fig. 2*A*, followed by Fig. 2 *B–E* representing MoS_2 treated by lithiation from the open circuit voltage around 2.1 to 1.8 ($x \approx 0.02$), 1.5 ($x \approx 0.07$), 1.2 ($x \approx 0.28$), and 1.1 V ($x \approx 0.85$) vs. Li^+/Li (Fig. 1*C*), respectively (these lithiation voltages are used for sampling throughout the entire paper). The films are polycrystalline with in-plane randomly oriented grains around 10 nm in size. As shown in our previous study, the special texture of vertically aligned MoS_2 maximally exposes the active edge sites on a 2D surface for HER and reduces the impedance of the charge transfer from the substrate to the surface sites, and at the same time fully opens van der Waals gaps for Li to be intercalated (43, 44). The morphologies of MoS_2 at potentials above ~1.5 V ($x < 0.1$) (TEM images in Fig. 2 *A–C*) have little change from Li intercalation. In comparison, some of the layers are obviously expanded and partially exfoliated at potentials below ~1.2 V ($x > 0.28$) (Fig. 2 *D* and *E*).

The layer spacing of MoS_2 nanofilms lithiated at different voltages is determined by averaging the layer spacing of randomly selected 15 grains in the TEM images (Fig. 2*F*). Pristine MoS_2 layer spacing is measured to be 6.45 Å, consistent with the previous study (49). The spacing of 1.8- and 1.5-V lithiation-treated MoS_2 is increased very little to 6.50 and 6.54 Å but still within the range of the error bar, indicating also very little expansion of van der Waals gap. Samples of 1.2 and 1.1 V are dramatically expanded to 7.25 and 7.21 Å, respectively, with increased layer spacing distribution. No other guest species observed in these TEM images rules out any organic intercalation (29, 50). Part of the intercalated Li reacts with ethanol and partially exfoliates MoS_2 layers, which is also responsible for the large layer spacing expansion (35, 42, 45, 51). Complete exfoliation happens with observed single layers when MoS_2 is treated by a deeper lithiation process (0.8 V) as illustrated in Fig. S2*A*. Note that the grains in 1.2- and 1.1-V lithiation-treated MoS_2 are expanded but not yet completely exfoliated or damaged after the lithiation process, and the morphology of vertically standing molecular layers is still maintained to a certain degree. Scanning electron microscopy (SEM) images of pristine and 1.1-V lithiation-treated MoS_2 shown in Fig. S3 also suggest that the film after lithiation treatment still maintains contact with the substrate except for partial detachment originated from the pinholes of the pristine film.

The Li electrochemical intercalation into van der Waals gap has at least three effects on the electronic structure of MoS_2. First, the layer spacing is increased after the lithiation and lithium–ethanol reaction processes, which changes the van der Waals interaction between adjacent layers and thus the electronic band structure (45, 52). Second, due to its highly reductive nature, the intercalated Li remaining from reaction with ethanol donates electrons to the MoS_2 slabs, which changes the d-band filling and oxidation state of Mo in MoS_2 as described by the schematic in Fig. 1*C* (29, 47, 48, 53, 54). Third, when the content of intercalated Li exceeds 0.28, the 2H semiconducting to 1T metallic MoS_2 phase transition happens. Both the oxidation state shift and phase transition of MoS_2 are observed in x-ray photoelectron spectroscopy (XPS) spectra in Fig. 3*A*. All of the spectra were calibrated by a carbon 1s peak located at 284.50 eV (55). Pristine MoS_2 shows a Mo $3d_{5/2}$ peak at 229.1 eV, indicating a +4 oxidation state of Mo (31). Before the 2H to 1T phase transition happens, Mo $3d_{5/2}$ binding energy is continuously shifted to 228.7 and 228.6 eV when MoS_2 is discharged to 1.8 and 1.5 V vs. Li^+/Li, respectively. The lower binding energies confirm our assumption that the intercalated Li donate electrons to MoS_2, resulting in lower oxidation states of

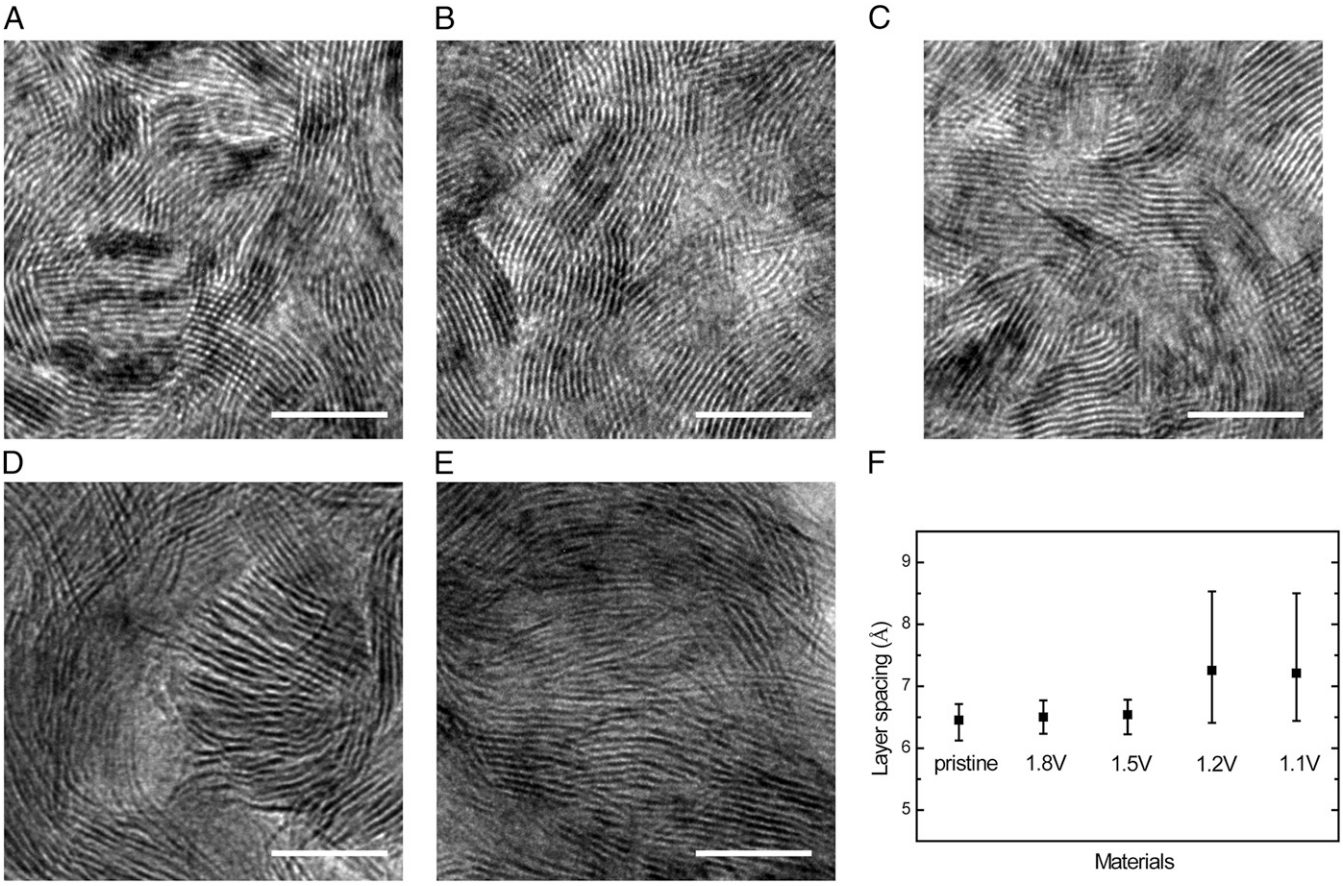

Fig. 2. TEM images of MoS_2 after Li intercalation. (*A*) TEM image of pristine MoS_2 with molecular layers perpendicular to the substrate. (*B–E*) TEM images of MoS_2 by Li electrochemical intercalation to 1.8, 1.5, 1.2, and 1.1 V vs. Li^+/Li, respectively. (*F*) Averaged layer spacing of pristine and lithiated MoS_2. Error bars represent the layer spacing variation of different grains measured in TEM images. Scale bar, 10 nm.

Mo (53, 54). Additional peaks start to appear when the 2H to 1T MoS_2 phase transition occurs through 1.2 to 1.1 V vs. Li^+/Li. Deconvolution of the broad Mo $3d_{5/2}$ and Mo $3d_{3/2}$ peaks in both spectra presents two independent Mo 3d regions, with a separation of binding energy around 0.8 eV (42, 51). The positions of deconvoluted Mo $3d_{5/2}$ peaks in both spectra are located at 229.0 and 228.2 eV, representing the 2H and 1T MoS_2 oxidation states, respectively. The composition of the 1T phase in MoS_2 nanofilm discharged to 1.1 V vs. Li^+/Li is increased compared with the one in the 1.2-V sample, which is indicated by the decreased ratio of 2H to 1T Mo $3d_{5/2}$ peak areas from 1.2 (1.53) to 1.1 V (0.86) shown in Fig. 3*A* (42, 51). Mo $3d_{5/2}$ peaks at 235.6 eV with +6 oxidation state are observed in 1.2- and 1.1-V lithiated MoS_2, suggesting the slight oxidation during the sample preparation. Fig. S4 shows that the oxidation states of S are maintained at −2 and not affected by Li intercalation when MoS_2 is discharged to 1.8 and 1.5 V. Additional peaks of S 2p region showing up at 1.2- and 1.1-V discharging voltage in Fig. S4 again confirm the 1T MoS_2 phase formation.

Raman spectra in Fig. 3*B* offer us more information about the morphology and phase transition of pristine and lithiated MoS_2. Fig. 3*C* illustrates the E_{1g}, E^1_{2g}, and A_{1g} vibration modes located at 281, 377, and 403 cm^{-1}, respectively, in pristine MoS_2 on MPGC with the calibration of Si peak at 520.0 cm^{-1} (ref. 56). The integrated intensity of A_{1g} is nearly three times that of E^1_{2g}, which suggests the texture of as-grown MoS_2 with molecular layers vertically standing on the substrate that favors the vibration of A_{1g} mode (43, 44). The 1.8- and 1.5-V lithiation-treated MoS_2 have nearly the same spectra with the pristine one, showing no phase or structure changes. As the content of intercalated Li is increased, more and more electrons are donated from Li to MoS_2 slabs, which results in the 2H to 1T phase transition to lower the Li_xMoS_2 electronic energy (29, 48, 53). Four additional peaks, located, respectively, at 197, 222, 335, and 349 cm^{-1}, indicate the 2H to 1T MoS_2 phase transition when MoS_2 was discharged to 1.2 and 1.1 V vs. Li^+/Li (35, 47, 48, 51). The increased intensities of the emerged peaks further confirm that 1.1-V discharged MoS_2 has more 1T phase than that in the 1.2-V sample.

Electrochemical Testing. Correlating the tunable layer spacing and electronic structure of MoS_2 by Li electrochemical intercalation and the corresponding HER catalytic activities offers clear insight (35, 42). The electrochemical testing of pristine and lithiated MoS_2 with mass loading around 22 μ g/cm^2 on MPGC were performed in 0.5 M H_2SO_4 solution with a typical three-electrode electrochemical cell setup (*Materials and Methods*). Before the polarization curve was tested the sample was cycled several times by taking continuous cyclic voltammograms (CVs) between −0.25 and 0.1 V vs. reversible hydrogen electrode (RHE) before iR correction to remove contaminants on the surface. Electrochemical impedance spectroscopy reveals negligible ohmic resistance of the films (Fig. S5). All of the results have been iR-corrected by subtracting the ohmic resistance loss from the overpotential. It turns out that MoS_2 HER activity can be continuously tuned by Li electrochemical intercalation to different voltages vs. Li^+/Li, as shown in Fig. 4 *A* and *B*. The pristine MoS_2 exhibits a Tafel slope of 123 mV per decade and an exchange current density of 3.4 × 10^{-3} mA/cm^2, showing comparably low HER catalytic activity (43).

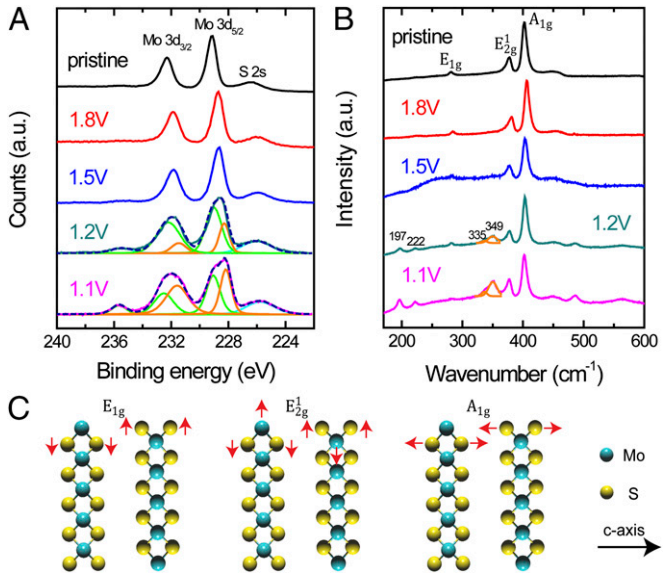

Fig. 3. Characterizations of pristine and lithiated MoS_2 nanofilms. (*A*) XPS spectra of pristine and Li electrochemically intercalated MoS_2. Mo 3d region is shifted toward lower binding energy after Li intercalation to 1.8 and 1.5 V vs. Li^+/Li. Mo $3d_{3/2}$ and $3d_{5/2}$ peaks are then split into two independent regions at 1.2 and 1.1 V vs. Li^+/Li, representing the 2H (green line) to 1T (orange line) MoS_2 phase transition. (*B*) Raman spectra of pristine and Li electrochemically intercalated MoS_2. Four additional peaks located at 197, 222, 335, and 349 cm^{-1} are observed in 1.2- and 1.1-V lithiated MoS_2, confirming the 1T phase MoS_2 formation. The broad peak left of the E^1_{2g} peak is deconvoluted into two peaks. (*C*) Atomic vibration direction of E_{1g}, E^1_{2g}, and A_{1g} Raman modes of MoS_2.

However, the Tafel slope is reduced to 84 and 60 mV per decade after MoS_2 is discharged to 1.8 and 1.5 V vs. Li^+/Li, respectively, before the 2H to 1T phase transition. The HER catalytic activity is then further improved by Li electrochemical intercalation to 1.2 and 1.1 V and saturated to a Tafel slope around 44 mV per decade, which agrees well with the exfoliated MoS_2 nanosheets by n-butyl Li solution (35). The 1.1-V lithiated MoS_2 has a slightly improved HER activity than that of 1.2 V. Deeper Li discharge process, for example 0.8 V vs. Li^+/Li lithiation, may completely exfoliate MoS_2 layers and destroy the bonds between the active material and the substrate upon exposure to aqueous electrolyte which performs degraded activity (Fig. S2*B*) (35, 45). Some previous studies suggested the reduction of MoS_2 to Mo metal and Li_2S when it was discharged to low potentials, which is another possibility to explain the activity degradation (45). Several identical samples at each lithiation voltages were tested to ensure the reproducibility of the results, as summarized in Table 1.

A high-surface-area 3D carbon fiber paper (CFP) was used to improve the overall HER performance of Li electrochemically intercalated MoS_2. Atomic layer deposition (ALD) is an established technique to deliver materials to high-aspect-ratio nanostructures in a conformal and ultrathin fashion (57–59). We conformally coated CFP with MoO_3 by ALD (*Materials and Methods*) (60), which was then converted to MoS_2 by the same rapid sulfurization process (the as-grown catalyst is donated as ALD MoS_2). The synthesis of ALD MoS_2 with molecular layers perpendicular to the substrate was confirmed by the TEM image and Raman spectrum shown in Fig. S6 *A* and *B*. Benefitting from the maximally exposed active edge sites, the thickness of MoS_2 nanofilm can be lowered down to reduce the loading of the catalyst while maintaining the high HER catalytic activity. Ten nm MoO_3 was deposited onto CFP and then converted to 10 nm MoS_2 with a mass loading around 120 μ g/cm^2. The HER catalytic activity of pristine ALD MoS_2 on CFP is shown in Fig. 4*A* with a Tafel slope of 98 mV per decade and exchange current density of 100×10^{-3} mA/cm^2 (Fig. S6*C*). The Tafel slope is dramatically improved to 44 mV per decade after discharging to

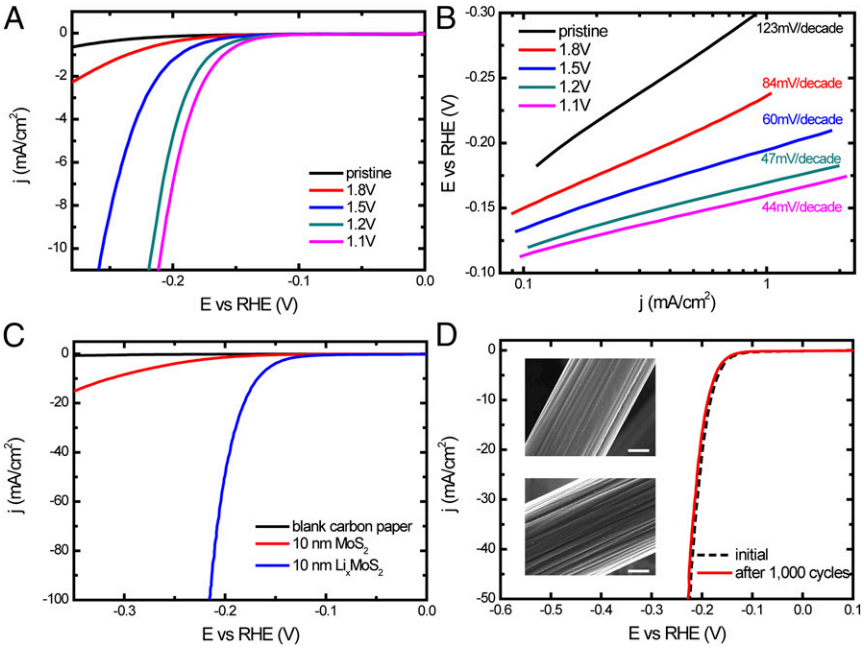

Fig. 4. Electrochemical characterization of pristine and lithiated MoS_2 on MPGC and CFP. (*A*) Polarization curves of pristine and lithiated MoS_2 on MPGC, with the catalytic activities improved by lower voltages Li intercalation. (*B*) Tafel slope of MoS_2 is continuously tuned by Li electrochemical intercalation to different voltages. The slope reaches around 44 mV per decade at 1.1 V vs. Li^+/Li. (*C*) HER activity of ALD MoS_2 on CFP is dramatically improved by Li intercalation. The Tafel slope is enhanced from 98 mV per decade (pristine MoS_2) to 44 mV per decade (lithiated MoS_2). (*D*) Electrochemical stability test of lithiated ALD MoS_2. The catalytic activity shows no obvious degradation after the cycling. (*Insets*) SEM images of the catalyst before (*Upper*) and after (*Lower*) 1,000 cycles showing no obvious change. Scale bar, 2 μ m.

Table 1. Electrochemical analysis of pristine and lithiated MoS_2 on MPGC

Materials	Tafel slope (mV per decade)	Exchange current density, 10^{-3} mA/cm^2	η (mV) @ j = 0.1 mA/cm^2	j (mA/cm^2) @ η = 200 mV
Pristine MoS_2	115~123	1.71~3.40	−173	−0.15
1.8 V MoS_2	75~86	0.80~1.62	−150	−0.40
1.5 V MoS_2	56~73	0.56~0.93	−133	−1.21
1.2 V MoS_2	46~51	0.10~0.38	−119	−4.96
1.1 V MoS_2	43~47	0.13~0.25	−113	−6.74

Tafel slopes and exchange current densities were obtained by several identical samples, and the overpotentials and cathodic current densities were obtained from Fig. 4*A*.

0.7 V vs. Li^+/Li, achieving much higher HER catalytic activity as shown in Fig. 4*C* and Fig. S6*C* (due to the different substrate and precursor used in the synthesis, the 1.2- and 1.1-V discharged ALD MoS_2 on CFP did not exhibit the best activity). Only 168- and 216-mV overpotentials (η) are needed for lithiated ALD MoS_2 to drive 10- and 100-mA/cm^2 cathodic current density (j), respectively. Electrochemical stability of the catalyst is of our concern as the Li intercalation process could introduce structure distortion and layer exfoliation, which can weaken the bond between ALD MoS_2 film and CFP substrate. The stability of lithiated ALD MoS_2 was tested by taking 1,000 continuous CV cycles between −0.19 and 0.1 V vs. RHE to reach 10 mA/cm^2 without iR correction. Fig. 4*D* shows that after 1,000 cycles the catalyst maintains high HER activity with negligible degradation. The SEM images of the catalyst before and after the cycling indicate that the film is intact. After the cycling test, 8.6% of Li was still maintained in the MoS_2 matrix (Table S1). In addition, stable electrocatalytic currents around 10 and 20 mA/cm^2 were observed for at least 5 h when constant voltages at 175 and 190 mV were applied to the catalyst, respectively (Fig. S6*D*). The MoS_2 molecular layers vertically standing on the substrate can create strong bonds to the surface, which is assumed to explain the good stability even after Li intercalation (44). In addition, the good stability demonstrates that 1T phase MoS_2 is maintained during the hydrogen evolution process (35, 42, 51).

Discussion

It is always important to construct the electronic structure–catalytic activity relationship in electrocatalysis (20, 37–41). As the H binding energy and activation barrier on the active edge sites are strongly related to the electronic structure of MoS_2 (20, 37), it is effective to continuously tune and improve the HER catalytic activity by continuously tuning the electronic structure, especially the oxidation state of Mo and 2H to 1T phase transition, through Li electrochemical intercalation. We find that even before the 2H to 1T phase transition occurs, HER activities are already improved along with the lowered oxidation states of Mo. The lowered oxidation states of Mo might have influence on the electron filling of bonding and antibonding between the active sites and H, which significantly changes the H bonding energy and activation barrier and thus improves the HER activity. Different from the recent studies in which MoS_2 and WS_2 are totally exfoliated to be monolayered nanosheets (35, 42), the morphology of MoS_2 in this study is not destroyed by Li intercalation and Li reaction with ethanol or water. Thus, we suspect that there is still Li trapped between the layers to anchor the oxidation state of Mo during the electrochemical test in which some of the intercalated Li could react with water to produce Li(OH) and H_2 (35, 42, 45, 51). Suggested by the improved HER activity of 1.1-V lithiated MoS_2 from 1.2 V, we also conclude that 1T MoS_2 shows superior HER activity to the 2H phase, which agrees with some recent results (35, 42). The XPS spectrum of 1.1-V lithiated MoS_2 before and after electrochemical cycling in Fig. S7 shows no obvious change in the 1T to 2H phase ratio, indicating that the electronic structure is maintained during hydrogen generation process (35, 42, 51). MoS_2 electronic structure changed by expanding the layers through Li intercalation and partial exfoliation, as shown in Fig. 2, could also be a possible explanation for the tunable HER activity (52, 54). In addition, Li intercalation improves the conductivity of MoS_2, which is also important to the improved HER activity of lithiated MoS_2.

In conclusion, we synthesized MoS_2 nanofilm with molecular layers perpendicular to the substrates. By Li electrochemical intercalation to different voltages vs. Li^+/Li, the layer spacing and electronic structure of MoS_2 was continuously tuned, thus tuning the HER catalytic activity effectively.

Materials and Methods

Material Synthesis and Li Intercalation. Molybdenum oxide layers were deposited by ALD on CFP (Fuel Cell Store) in a customized ALD–ozone system. Molybdenum hexacarbonyl (99.9%, Sigma-Aldrich) was used as the molybdenum precursor. Ozone was generated from a mixture of oxygen (99.99%) and nitrogen (99.998%, with mixing concentration of 50 ppm) in an ozone generator (MKS, AX8407-C2). The feeding oxygen flow rate was kept at ~500 standard cubic centimeters per minute (sccm), providing an ozone concentration of 21.7 wt %. The ozone flow into the chamber was controlled by a mass flow controller at 200 sccm. The substrate temperature was kept at 165 °C, the molybdenum precursor at 60 °C, and ozone feed line at 120 °C. An exposure mode was adopted for deposition on carbon papers. The molybdenum precursor were exposed for 0.5 s and soaked in the chamber for another 1 s via a stop valve before argon (99.999%) purging. The growth rates and thickness of the films were calibrated by 10 cm × 10 mm witness silicon pieces (P-type test wafer 0–100 Ω-cm 500 μm single-sided polished, University Wafer). For ALD on CFP, weight changes were also tracked as a function of ALD cycle numbers to provide complementary information about the growth rate. From the witness wafer piece, the coated CFP in this article was expected to have an average film thickness of 100 ± 5. Å The surface area of CFP was calculated to be 29 cm^2/cm^2. To verify conformal coating, Auger element mapping was conducted on the molybdenum-oxide-coated CFP shown in Fig. S8. By comparing the SEM images before and after ALD as shown by Fig. S8 *A* and *B*, there were no drastic morphology changes during the deposition process. The element mapping shown in Fig. S8 *C*–*E* confirmed that Mo and O are uniformly distributed.

Edge-terminated MoS_2 nanofilms on MPGC (HTW Hochtemperatur Werkstoffe Gmbh) and CFP were grown inside a single-zone, 12-inch horizontal tube furnace (Lindberg/Blue M) equipped with a 1-inch-diameter quartz tube. The substrates coated with Mo or MoO_3 thin films were placed at the hot center of the tube furnace. Sulfur powder (99.99%, Sigma Aldrich) was placed on the upstream side of the furnace at carefully adjusted locations to set the temperature. Ar gas was used as the precursor carrier and the pressure and flow rate were kept at 1,000 mtorr and 100 sccm, respectively, during the growth. The heating center of the furnace was quickly raised to reaction temperature of 600 °C in 20 min, and the sulfur precursor was kept at around 200 °C. The furnace was held at reaction temperature for 10 min, followed by natural cool-down.

The as-grown MoS_2 was then made into a battery configuration acting as the cathode, combined with Li metal as anode and 1.0 M $LiPF_6$ in 1:1 wt/wt ethylene carbonate/diethyl carbonate (EMD Chemicals) as electrolyte. The galvanostatic discharge currents for MoS_2 samples were set at 200 mA/g. After the discharge process, samples were cleaned by ethanol to remove the electrolyte on the surface. ICP-MS samples were prepared in 5% HNO_3 solution by taking continuous CV cycles between 0 and 1.2 V vs. a saturated calomel electrode (SCE) to oxidize and dissolve Li and Mo into the solution.

Characterizations. Characterizations were carried out using TEM (FEI Tecnai G2 F20 X-Twin microscope at 200 keV), Raman spectroscopy (531-nm

excitation laser, cutoff around 175 cm^{-1}, WITEC Raman spectrometer), XPS [SSI SProbe XPS spectrometer with Al(K_a) source], SEM (FEI Nova NanoSEM 450), and Auger electron spectroscopy (PHI 700 Scanning Auger Nanoprobe).

Electrochemical Measurements. MoS_2 nanofilms on MPGC and CFP were tested in 0.5 M H_2SO_4 solution (deaerated by N_2) using a typical three-electrode electrochemical cell setup, with an SCE [E(RHE) = E(SCE) + 0.280 V after calibration] as the reference electrode and a graphite rod (99.999%, Sigma-Aldrich) as the counter electrode. Electrochemically inert wax (Apiezon wax W-W100) and kapton tape were used to define the 1-cm^2 electrode area. Linear sweep voltammetry (scan rate 2 mV/s), CV (scan rate 100 mV/s), and ac impedance spectroscopy (at zero overpotential) were recorded by a Biologic VSP potentiostat.

ACKNOWLEDGMENTS. We acknowledge support by the Department of Energy, Office of Basic Energy Sciences, Materials Sciences and Engineering Division, under Contract DE-AC02-76-SFO0515. This work was also supported as part of the Center on Nanostructuring for Efficient Energy Conversion at Stanford University, an Energy Frontier Research Center funded by the US Department of Energy, Office of Science, Office of Basic Energy Sciences under Award DE-SC0001060.

1. Novoselov KS, et al. (2004) Electric field effect in atomically thin carbon films. *Science* 306(5696):666–669.
2. Zhang Y, Tan Y-W, Stormer HL, Kim P (2005) Experimental observation of the quantum Hall effect and Berry's phase in graphene. *Nature* 438(7065):201–204.
3. Stankovich S, et al. (2006) Graphene-based composite materials. *Nature* 442(7100): 282–286.
4. Li X, Wang X, Zhang L, Lee S, Dai H (2008) Chemically derived, ultrasmooth graphene nanoribbon semiconductors. *Science* 319(5867):1229–1232.
5. Novoselov KS, et al. (2005) Two-dimensional atomic crystals. *Proc Natl Acad Sci USA* 102(30):10451–10453.
6. Koski KJ, Cui Y (2013) The new skinny in two-dimensional nanomaterials. *ACS Nano* 7(5):3739–3743.
7. Butler SZ, et al. (2013) Progress, challenges, and opportunities in two-dimensional materials beyond graphene. *ACS Nano* 7(4):2898–2926.
8. Coleman JN, et al. (2011) Two-dimensional nanosheets produced by liquid exfoliation of layered materials. *Science* 331(6017):568–571.
9. Tenne R (2003) Advances in the synthesis of inorganic nanotubes and fullerene-like nanoparticles. *Angew Chem Int Ed Engl* 42(42):5124–5132.
10. Geim AK (2009) Graphene: Status and prospects. *Science* 324(5934):1530–1534.
11. Radisavljevic B, Radenovic A, Brivio J, Giacometti V, Kis A (2011) Single-layer MoS_2 transistors. *Nat Nanotechnol* 6(3):147–150.
12. Zhan Y, Liu Z, Najmaei S, Ajayan PM, Lou J (2012) Large-area vapor-phase growth and characterization of $MoS_{(2)}$ atomic layers on a $SiO_{(2)}$ substrate. *Small* 8(7):966–971.
13. Mizushima K, Jones PC, Wiseman PJ, Goodenough JB (1980) Li_xCoO_2 ($0<x<-1$): A new cathode material for batteries of high energy density. *Mater Res Bull* 15(6):783–789.
14. Shu ZX, McMillan RS, Murray JJ (1993) Electrochemical intercalation of lithium into graphite. *J Electrochem Soc* 140(4):922–927.
15. Zhang H, et al. (2009) Topological insulators in Bi_2Se_3, Bi_2Te_3 and Sb_2Te_3 with a single Dirac cone on the surface. *Nat Phys* 5(6):438–442.
16. Peng H, et al. (2010) Aharonov-Bohm interference in topological insulator nanoribbons. *Nat Mater* 9(3):225–229.
17. Kong D, et al. (2010) Topological insulator nanowires and nanoribbons. *Nano Lett* 10(1):329–333.
18. Poudel B, et al. (2008) High-thermoelectric performance of nanostructured bismuth antimony telluride bulk alloys. *Science* 320(5876):634–638.
19. McKone JR, Pieterick AP, Gray HB, Lewis NS (2013) Hydrogen evolution from Pt/Ru-coated p-type WSe_2 photocathodes. *J Am Chem Soc* 135(1):223–231.
20. Hinnemann B, et al. (2005) Biomimetic hydrogen evolution: MoS_2 nanoparticles as catalyst for hydrogen evolution. *J Am Chem Soc* 127(15):5308–5309.
21. Jaramillo TF, et al. (2007) Identification of active edge sites for electrochemical H_2 evolution from MoS_2 nanocatalysts. *Science* 317(5834):100–102.
22. Huang X, et al. (2013) Solution-phase epitaxial growth of noble metal nanostructures on dispersible single-layer molybdenum disulfide nanosheets. *Mol Ther* 4:1444.
23. Farrington GC, Briant JL (1979) Fast ionic transport in solids. *Science* 204(4400): 1371–1379.
24. Whittingham MS (1978) Chemistry of intercalation compounds: Metal guests in chalcogenide hosts. *Prog Solid State Chem* 12(1):41–99.
25. Whittingham MS (1976) The role of ternary phases in cathode reactions. *J Electrochem Soc* 123(3):315–320.
26. Koski KJ, et al. (2012) High-density chemical intercalation of zero-valent copper into Bi_2Se_3 nanoribbons. *J Am Chem Soc* 134(18):7584–7587.
27. Koski KJ, et al. (2012) Chemical intercalation of zerovalent metals into 2D layered Bi_2Se_3 nanoribbons. *J Am Chem Soc* 134(33):13773–13779.
28. Yoo E, et al. (2008) Large reversible Li storage of graphene nanosheet families for use in rechargeable lithium ion batteries. *Nano Lett* 8(8):2277–2282.
29. Py MA, Haering RR (1983) Structural destabilization induced by lithium intercalation in MoS_2 and related compounds. *Can J Phys* 61(1):76–84.
30. Chen Z, et al. (2011) Core-shell MoO_3-MoS_2 nanowires for hydrogen evolution: A functional design for electrocatalytic materials. *Nano Lett* 11(10):4168–4175.
31. Kibsgaard J, Chen Z, Reinecke BN, Jaramillo TF (2012) Engineering the surface structure of MoS_2 to preferentially expose active edge sites for electrocatalysis. *Nat Mater* 11(11):963–969.
32. Li Y, et al. (2011) MoS_2 nanoparticles grown on graphene: An advanced catalyst for the hydrogen evolution reaction. *J Am Chem Soc* 133(19):7296–7299.
33. Merki D, Hu X (2011) Recent developments of molybdenum and tungsten sulfides as hydrogen evolution catalysts. *Energy Environ Sci* 4(10):3878–3888.
34. Vrubel H, Merki D, Hu X (2012) Hydrogen evolution catalyzed by MoS_3 and MoS_2 particles. *Energy Environ Sci* 5(3):6136–6144.
35. Lukowski MA, et al. (2013) Enhanced hydrogen evolution catalysis from chemically exfoliated metallic MoS_2 nanosheets. *J Am Chem Soc* 135(28):10274–10277.
36. Karunadasa HI, et al. (2012) A molecular MoS_2 edge site mimic for catalytic hydrogen generation. *Science* 335(6069):698–702.
37. Bollinger MV, Jacobsen KW, Norskov JK (2003) Atomic and electronic structure of MoS_2 nanoparticles. *Phys Rev B* 67(8):085410-1–085410-17.
38. Kanan MW, et al. (2010) Structure and valency of a cobalt-phosphate water oxidation catalyst determined by in situ X-ray spectroscopy. *J Am Chem Soc* 132(39):13692–13701.
39. Vojvodic A, Nørskov JK (2011) Chemistry. Optimizing perovskites for the water-splitting reaction. *Science* 334(6061):1355–1356.
40. Subbaraman R, et al. (2012) Trends in activity for the water electrolyser reactions on 3d M(Ni,Co,Fe,Mn) hydr(oxy)oxide catalysts. *Nat Mater* 11(6):550–557.
41. Suntivich J, May KJ, Gasteiger HA, Goodenough JB, Shao-Horn Y (2011) A perovskite oxide optimized for oxygen evolution catalysis from molecular orbital principles. *Science* 334(6061):1383–1385.
42. Voiry D, et al. (2013) Enhanced catalytic activity in strained chemically exfoliated WS_2 nanosheets for hydrogen evolution. *Nat Mater* 12(9):850–855.
43. Kong D, et al. (2013) Synthesis of MoS_2 and $MoSe_2$ films with vertically aligned layers. *Nano Lett* 13(3):1341–1347.
44. Wang H, et al. (2013) $MoSe_2$ and WSe_2 nanofilms with vertically aligned molecular layers on curved and rough surfaces. *Nano Lett* 13(7):3426–3433.
45. Zeng Z, et al. (2011) Single-layer semiconducting nanosheets: High-yield preparation and device fabrication. *Angew Chem Int Ed Engl* 50(47):11093–11097.
46. Imanishi N, Toyoda M, Takeda Y, Yamamoto O (1992) Study on lithium intercalation into MoS_2. *Solid State Ion* 58(3–4):333–338.
47. Julien CM (2003) Lithium intercalated compounds: Charge transfer and related properties. *Mater Sci Eng Rep* 40(2):47–102.
48. Yang D, Sandoval SJ, Divigalpitiya WMR, Irwin JC, Frindt RF (1991) Structure of single-molecular-layer MoS_2. *Phys Rev B Condens Matter* 43(14):12053–12056.
49. Chen J, Kuriyama N, Yuan H, Takeshita HT, Sakai T (2001) Electrochemical hydrogen storage in MoS_2 nanotubes. *J Am Chem Soc* 123(47):11813–11814.
50. Divigalpitiya WM, Frindt RF, Morrison SR (1989) Inclusion systems of organic molecules in restacked single-layer molybdenum disulfide. *Science* 246(4928):369–371.
51. Eda G, et al. (2011) Photoluminescence from chemically exfoliated MoS_2. *Nano Lett* 11(12):5111–5116.
52. Frey GL, Elani S, Homyonfer M, Feldman Y, Tenne R (1998) Optical-absorption spectra of inorganic fullerenelike MS_2 (M=Mo, W). *Phys Rev B* 57(11):6666–6671.
53. Rocquefelte X, et al. (2000) Mo cluster formation in the intercalation compound $LiMoS_2$. *Phys Rev B* 62(4):2397–2400.
54. Wu S, et al. (2012) Electrochemically reduced single-layer MoS_2 nanosheets: characterization, properties, and sensing applications. *Small* 8(14):2264–2270.
55. Moulder JF, Stickle WF, Sobol PE, Bomben KD (1995) *Handbook of X-ray Photoelectron Spectroscopy* (ULVAC-PHI, Inc., Chigasaki, Japan; Physical Electronics USA, Inc., Chanhassen, MN), pp 40–41.
56. Li B, Yu D, Zhang S-L (1999) Raman spectral study of silicon nanowires. *Phys Rev B* 59(3):1645–1648.
57. Elam JW, Dasgupta NP, Prinz FB (2011) ALD for clean energy conversion, utilization, and storage. *MRS Bull* 36(11):899–906.
58. Leskela M, Ritala M (2002) Atomic layer deposition (ALD): From precursors to thin film structures. *Thin Solid Films* 409(1):138–146.
59. Dasgupta NP, Liu C, Andrews S, Prinz FB, Yang P (2013) Atomic layer deposition of platinum catalysts on nanowire surfaces for photoelectrochemical water reduction. *J Am Chem Soc* 135(35):12932–12935.
60. Diskus M, Nilsen O, Fjellvag H (2011) Growth of thin films of molybdenum oxide by atomic layer deposition. *J Mater Chem* 21(3):705–710.